Journal of Power Sources 208 (2012) 306–315

Contents lists available at SciVerse ScienceDirect

Journal of Power Sources

journal homepage: www.elsevier.com/locate/jpowsour

Carbon monoxide and methanol oxidation on potential-modified Pt–Ru/C electrocatalyst for polymer electrolyte fuel cells

Amado Velázquez-Palenzuela, Enric Brillas, Conchita Arias, Francesc Centellas, José Antonio Garrido, Rosa María Rodríguez, Pere-Lluís Cabot*

Laboratori d'Electroquímica dels Materials i del Medi Ambient, Departament de Química Física, Universitat de Barcelona, Martí i Franquès 1-11, 08028 Barcelona, Spain

ARTICLE INFO

Article history:
Received 30 November 2011
Received in revised form 10 February 2012
Accepted 17 February 2012
Available online 25 February 2012

Keywords:
Pt–Ru nanoparticles
Electrocatalysis
Methanol oxidation reaction
Anodic treatment
Hydrous ruthenium oxide

ABSTRACT

In this paper, the effect of the anodic treatment of carbon-supported Pt–Ru nanoparticles using a HP 20% 1:1 Pt–Ru alloy on Vulcan XC-72 carbon black on the CO stripping and methanol oxidation reaction (MOR) has been analyzed. Thin-layer electrodes were prepared by depositing catalyst inks of Pt–Ru/C and Nafion on glassy carbon (GC) disks. Steady-state polarization at potentials >1.00 V vs. RHE in 0.5 M H_2SO_4 was used for the electrochemical activation of the specimen. Cyclic voltammetry was applied for electrochemical testing. The morphological analysis was performed by transmission electron microscopy (TEM), energy dispersive X-ray (EDX), selected-area electron diffraction (SAED), and Fast Fourier Transform (FFT). The present results showed that the anodic potential treatment causes Ru segregation with some carbon oxidation and agglomeration of nanoparticles. Activation of CO and methanol oxidation was found, indicating the production of the beneficial hydrous Ru oxide, RuO_xH_y, the promoting species for both reactions. For the MOR, the optimum potential of anodic treatment was located at 1.40–1.60 V. An apparent double Tafel slope behavior with values of 120 and 200 mV dec^{-1} was obtained after this optimum potential treatment, which was tentatively attributed to the existence of two different active sites for the MOR.

1. Introduction

Fuel cells have been proposed as capable energy generator devices, for example polymer electrolyte fuel cells (PEFCs), which can employ proton-exchange polymeric membranes as electrolyte [1–8]. The benefits of this kind of energy-supply system consist in a low working temperature, high energy conversion and energy density, low or practically insignificant production of contaminating exhaust, and miniaturization possibilities allowing its incorporation in portable electronic devices. For many years, hydrogen and methanol, the latter for direct methanol fuel cells (DMFCs) [9], have been used as fuels with good results. The oxidation reactions of both reagents take place according to the following reactions:

$$H_2 \rightarrow 2H^+ + 2e^- \quad (1)$$

$$CH_3OH + H_2O \rightarrow 6H^+ + 6e^- + CO_2 \quad (2)$$

Pt nanoparticles supported on high surface carbon materials have been employed as electrocatalysts for the fuel oxidation, thus allowing reducing the loading of the expensive Pt. Nevertheless, the wide commercialization of PEFCs is severely limited by the problem of the CO poisoning [10]. Thus, the low-cost hydrogen produced from reforming contains CO as impurity. In the case of the DMFCs, the alcohol oxidation leads to the generation of CO as intermediate. This molecule remains chemisorbed on the surface of the Pt nanoparticles, thus blocking the active sites for the fuel oxidation and causing a dramatic efficiency loss of the fuel cell performance. To solve the problem, Pt–Ru electrocatalysts which present a much better CO tolerance have been developed. In this system, it is proposed a bifunctional mechanism in which the Ru atoms of the anode surface are oxidized to form hydroxylated species (Ru–OH) from water discharge by reaction (3) [11,12]:

$$Ru + H_2O \rightarrow Ru\text{–}OH + e^- + H^+ \quad (3)$$

and then, the Ru–OH species are an oxygen source for the CO oxidation from reaction (4):

$$Ru\text{–}OH + Pt\text{–}CO \rightarrow Pt + Ru + CO_2 + e^- + H^+ \quad (4)$$

An additional explanation for the better performance of Pt–Ru nanoparticles is based on a weakening of the Pt–CO bond because of an electronic modification by the incorporated Ru atoms [13]. According to the above mechanisms, several researchers have studied the optimum Pt–Ru composition that leads to the higher CO and

* Corresponding author. Tel.: +34 93 4039236; fax: +34 93 4021231.
E-mail address: p.cabot@ub.edu (P.-L. Cabot).

0378-7753/$ – see front matter © 2012 Elsevier B.V. All rights reserved.
doi:10.1016/j.jpowsour.2012.02.064

methanol oxidation efficiency. Thus, considering the reaction (4), an equiatomic composition seems to be the suitable stoichiometry. This was the result found by Arico et al. in the case of DMFC at 130 °C [14], but there is no general agreement because a wide range of intermediate Pt–Ru ratios have been reported as optimal, depending on the preparation conditions [15–19]. These discrepancies indicate that the speciation of Ru in the electrocatalyst must be taken into account. Especial attention has been focused on Ru oxides, mainly the hydrous RuO_2 (RuO_xH_y) [20–39]. Some researchers, as Rolison et al. [32], postulated that the alloy formation is not needed and the true promotional effect is caused by the properties of RuO_xH_y. Although this oxide is not active for the CO or methanol oxidation [24,29,34,35], it can act as a mixed proton/electron conductor [32,36] and can also work as catalyst for the oxygen chemisorption, properties not shown by the anhydrous oxide [24]. Besides, the favored formation of the proton-conducting hydroxylated oxide allows a better fuel-electrocatalyst reaction and the ionomer fraction in the catalyst layer can be reduced [37]. Typically, amorphous RuO_xH_y species appear in the as-prepared Pt–Ru/C electrocatalyst [20,22,29,34], as indicated by transmission electron microscopy (TEM) and X-ray diffraction (XRD) analyses. Taking into account such properties, it seems that an intimate contact between RuO_xH_y and crystalline Pt nanoparticles is preferred for achieving the best electrocatalytic properties.

Some authors have considered the use of potential treatments, mainly through cyclic voltammetry (CV), in order to modify original Pt–Ru electrocatalysts through generation of oxides that can improve the methanol oxidation reaction (MOR) [26,28]. It is generally accepted that setting high anodic limits for the potential scan, greater than 1.00–1.20 V, metallic oxides are irreversibly formed [31]. Ru dissolution has also been proposed, because the cyclic voltammogram profiles become similar to those of Pt [20,23,31], although it is not clear whether this modification is caused by the Ru loss from the nanoparticle surface or by the change in the oxidation state of the Ru atoms [31]. Rose et al. [33], using X-ray absorption spectroscopy (XAS), found that Ru species were not dissolved after holding the potential at 1.20 V for 3 h, thus suggesting that the Ru oxides could be retained on the surface of the nanoparticles. The effect of the potential treatment on the improvement of the MOR has been analyzed by potential cycling with high anodic limits ($E > 1.00$ V). The best performance was found in the range 1.10–1.40 V, the MOR enhancement being explained by the formation of RuO_xH_y during this treatment [26,28]. A similar behavior has been reported in a previous work of our group [39], in which a maximum increase of 180% in the MOR activity after 100 voltammetric cycles with 1.00 V as the anodic limit was achieved. The modification of the alloy degree by activation has also been proposed, but the possible effect was found negligible [28]. In this case, a steady-state polarization was used as the faster procedure for carrying out the electrocatalyst activation. Nevertheless, we have not found any paper in the literature employing anodic potential treatments to activate Pt–Ru electrocatalysts for CO oxidation. Besides, the effect of the potential step duration on the electrocatalyst morphology has not been considered.

To gain a better understanding of the phenomena that take place during the potential activation step, this paper studies the effect of the anodic treatment on a carbon-supported Pt–Ru electrocatalyst (Pt–Ru/C) and the oxidation of both, CO and methanol. Steady-state polarizations at potentials >1.00 V for different periods were applied using the thin-layer electrode technique, in which small amounts of electrocatalyst with Nafion are deposited on glassy carbon (GC) [40]. Cyclic voltammetry was employed for the electrochemical study of the modified nanoparticles, as well as for CO stripping and MOR testing. After the treatment, TEM observation, energy-dispersive X-ray (EDX) analysis, Fast Fourier Transform (FFT) and selected-area electron diffraction (SAED) were used for the structural characterization.

2. Experimental

2.1. Materials and reagents

High performance (HP) 20% 1:1 Pt–Ru alloy on Vulcan XC-72 carbon black (Pt–Ru/C electrocatalyst, actual analysis giving 19.9 wt.% Pt–Ru) and HP 20% Pt supported on carbon Vulcan XC-72 (Pt/C electrocatalyst, actual analysis giving 19.6 wt.% Pt on carbon), required for comparative purposes, were purchased from E–Tek. The ionomer was a 5% solution of Nafion perfluorinated ion-exchange resin in a mixture of aliphatic low molecular weight alcohols (isopropanol:*n*-propanol in weight ratio 55:45) and water (15–25 wt.% in the mixture) supplied by Aldrich. GC disk electrode of 3 mm diameter was provided by Metrohm. Analytical grade 96% H_2SO_4 from Merck was used to prepare 0.5 M H_2SO_4 as the background electrolyte for the CV and CO stripping experiments. Besides, analytical grade 99.9% methanol from Panreac was employed for the elaboration of the 0.5 M H_2SO_4 + 1.0 M CH_3OH solution to carry out the methanol oxidation trials. All solutions were prepared with high-purity water obtained with a Millipore Milli-Q system (resistivity > 18 MΩ cm). Ar gas was Linde 5.0 (purity ≥ 99.999%), while CO gas was Linde 3.0 (purity ≥ 99.9%).

2.2. Electrode preparation

Aqueous slurries with 5.0 mg ml^{-1} electrocatalyst were prepared by sonicating for 45 min appropriate amounts of Pt–Ru/C or Pt/C electrocatalyst and the ionomer solution. The Nafion composition in the catalyst ink was controlled in order to obtain in the dried inks a Nafion fraction of 25–30 wt.%, which was found in previous works [38] as the optimum ink composition that exposes the highest electroactive surface area. About 2.5–3.0 μl of the homogeneous ink were deposited by means of a digital micropipette on the surface of the GC disk electrode, carefully weighting the deposited volumes with an AG 245 Mettler-Toledo analytical balance (accuracy of ±0.01 mg). The prepared electrodes were dried for 24 h in a clean dessicator at room temperature and further, they were coupled to an Ecochemie Autolab RDE to be used as working electrodes of the electrochemical trials. The final Pt loads on the GC surface were 32 ± 3 μg cm^{-2}. Previously to the ink deposition, the GC tip was consecutively polished with aluminum oxide pastes of 0.3 and 0.05 μm (Buehler Micropolish II deagglomerated α-alumina and γ-alumina, respectively) on a Buehler PSA-backed White Felt polishing cloth until achieving a mirror finish, being rinsed with Millipore Milli-Q water in an ultrasonic bath between the polishing steps. The GC coverage by the Pt–Ru/Nafion ink approached 100%.

2.3. Electrochemical measurements

All the electrochemical experiments were performed with a conventional thermostated double wall three-electrode glass cell from Metrohm of 200 ml capacity and an Ecochemie Autolab PGSTAT100 potentiostat–galvanostat with computerized control by an Autolab Nova 1.4 software. A Pt rod of 3.78 cm^2 apparent area was used as the auxiliary electrode and a double junction Ag|AgCl|KCl (saturated) electrode was employed as the reference electrode. All potentials given in this work are referred to the reversible hydrogen electrode (RHE) in the working electrolyte. The electrolyte was firstly deaerated by bubbling Ar for 30 min and further, 15 cyclic voltammograms at 100 mV s^{-1}, 15 more at 50 mV s^{-1}

and 10 more at 20 mV s^{-1} between 0.02 and 1.00 V were consecutively performed under Ar atmosphere at 25.0 °C. The recorded cyclic voltammograms were practically quasi-stationary after the second cycle, evidencing the stability and cleanness of the electrodes.

Anodic potential treatments of the Pt–Ru/C electrocatalyst were made by steady-state polarization of the prepared electrode in an Ar-deaerated 0.5 M H_2SO_4 solution at potentials of 0.00–1.80 V within times of 1–3600 s. Nevertheless, CO and methanol oxidation reactions were focused in the high potential region (E > 1.00 V), where a noticeable promotional effect was detected. Cyclic voltammograms and CO stripping experiments were conducted at 25.0 °C under Ar atmosphere at 20 mV s^{-1}. In the latter case, the electrode was previously prepared by bubbling CO through the solution for at least 15 min and keeping the electrode potential at 0.01 V to assure the complete adsorption of CO on its surface. The CO remaining in the electrolyte was further removed by Ar bubbling for 30 min. For the anodically treated specimens, their activation was carried out after a first CO stripping experiment. Later, a second CO trial was conducted in the same electrolyte following the above methodology.

The methanol oxidation reactions in the different anodically treated Pt–Ru/C electrocatalysts were studied in a 0.5 M H_2SO_4 + 1.0 M CH_3OH solution, which was previously deaerated by sparging Ar for 30 min and an Ar flow was kept over it during the potential cycling. Cyclic voltammograms between 0.00 and 0.65 V at 20 mV s^{-1} and 25.0 °C were recorded in the acidic methanol solution. After a first experiment, the electrode was washed with Millipore Milli-Q water, dried and transferred to a cell containing Ar-deaerated 0.5 M H_2SO_4, where the activation step took place. Following this, the working electrode was used again for the alcohol oxidation in 0.5 M H_2SO_4 + 1.0 M CH_3OH solution. Control experiments without anodic potential treatment were also tested confirming that the consecutive use of an electrode did not cause any loss of catalyst loading.

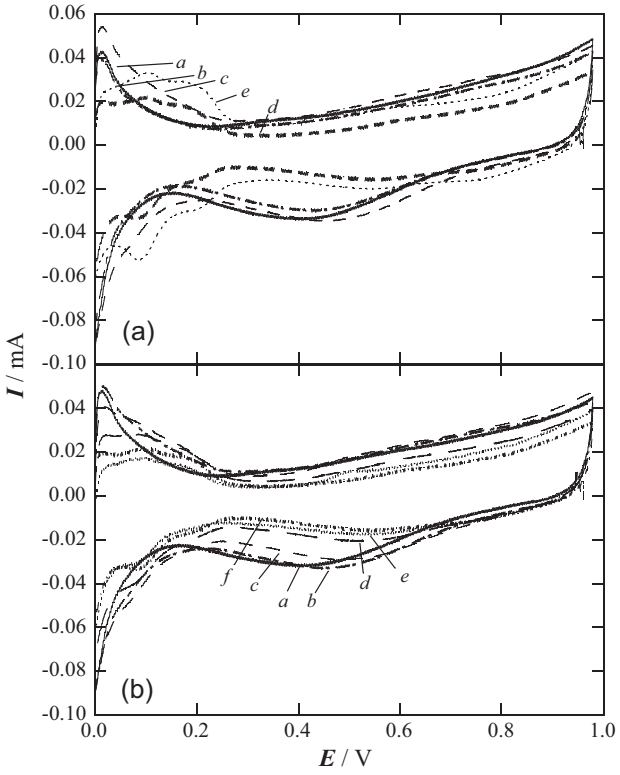

Fig. 1. Cyclic voltammograms recorded for the HP 20% 1:1 Pt–Ru/C Vulcan XC-72 electrocatalyst anodically treated in 0.5 M H_2SO_4 at 20 mV s^{-1} and 25.0 °C. In plot (a), the electrocatalyst was anodically treated during 1800 s at (*b*) 1.00 V, (*c*) 1.20 V, (*d*) 1.40 V and (*e*) 1.60 V. The polarization curve corresponding to (*a*) the untreated HP 20% 1:1 Pt–Ru/C Vulcan XC-72 electrocatalyst is also displayed. In plot (b), the results for the anodic treatment of the electrocatalyst at 1.40 V for (*b*) 1 s, (*c*) 10 s, (*d*) 100 s, (*e*) 300 s and (*f*) 1800 s are displayed, as well as the corresponding to the untreated HP 20% 1:1 Pt–Ru/C Vulcan XC-72 electrocatalyst. Catalyst ink with 30 μg Pt cm^{-2} and Nafion 30 wt.%.

2.4. Structural analysis

For physical characterization, transmission electron microscopy (TEM), high-resolution TEM (HRTEM), energy dispersive X-ray analysis (EDX), selected-area electron diffraction (SAED) and Fast Fourier Transform (FFT) were employed in this work. These techniques were performed using a JEOL JEM 2100 TEM 200 kV microscope, which allowed obtaining the corresponding images and the EDX spectra as well as the electron diffraction pattern. FFT algorithm was applied to the HRTEM images. For these analyses, the HP 20% 1:1 Pt–Ru/C Vulcan XC-72 electrocatalyst was supported on a GC electrode and anodically treated as described above. After the activation process, the electrode was extracted, washed with Millipore Milli-Q water, dried, and placed in a vial with 0.5–1.0 ml of *n*-hexane covered with parafilm, which was introduced in an ultrasonic bath for 10 min to release the electrocatalyst from the GC surface. Then, the remaining suspension was stirred for other 10 min and a drop of it was placed over a holley-carbon copper grid (400 mesh), being its solvent evaporated using a 40 W lamp for 15 min. TEM and HRTEM images were recorded with a Gatan MultiScan 794 CCD (charge-coupled device) camera. A Gatan Digital Micrograph 3.7.0 software was used for the digital treatment of images and SAED analysis. Crystallographic data obtained from electron diffraction pattern were contrasted with a CaRIne Cristallography 3.1 software and a PCPDFWIN 2.3 database. The Oxford INCAEnergy software was applied to the EDX spectra for the quantitative analysis of the material.

X-ray photoelectron spectroscopy (XPS) experiments for the anodically treated Pt–Ru/C electrocatalysts were performed using a Physical Electronics PHI 5500 Multitechnique System spectrometer with a monochromatic X-ray source (Aluminium–Kα line of 1486.6 eV energy and 350 W). This X-ray source was placed perpendicularly to the analyzer axis and calibrated using the 1s line of the C region located at 284.6 eV. The analyzed area was a circle of 0.8 mm diameter. The sample was deposited from a suspension in *n*-hexane, following the same methodology employed for the TEM analyses. A survey spectrum (187.5 eV of Pass Energy and 0.8 eV/step) was obtained before recording the high-resolution spectra (23.5 eV of Pass Energy and 0.1 eV/step). All measurements were made in ultra high vacuum chamber pressure between 5.0×10^{-9} and 2.0×10^{-8} Torr. The XPS spectra were analyzed using an Ulvac-phi MultiPak V8.2B software.

3. Results and discussion

3.1. Cyclic voltammetry in 0.5 M H_2SO_4 after anodic treatment

Fig. 1a shows the cyclic voltammograms recorded for the Pt–Ru/C electrocatalyst anodically treated at 1.00, 1.20, 1.40 and 1.60 V during 1800 s, whereas Fig. 1b presents the cyclic voltammograms for the Pt–Ru/C electrocatalyst after treatment at 1.40 V during 1, 10, 100, 300 and 1800 s. The *I–E* curves were found to be reproducible and stationary after the anodic treatment and they were not altered after several potential scans, thus proving the stability of the electrocatalyst surface layer. In particular, this means that the formation of the Ru oxides is an irreversible process. It can be observed from plots in Fig. 1 that the increase of the applied

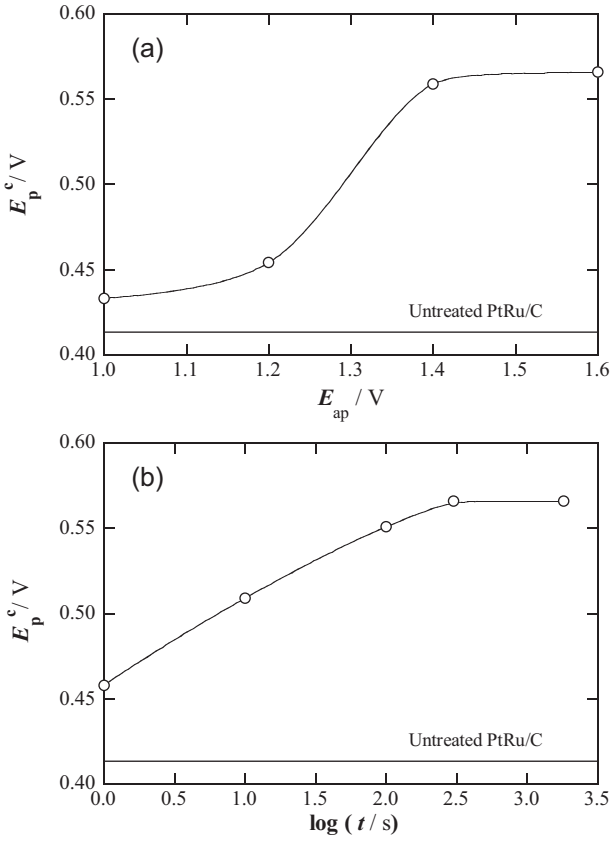

Fig. 2. Variation of the cathodic peak potential of the cyclic voltammograms of Fig. 1 with: (a) the applied anodic potential during 1800 s and (b) the logarithm of the step potential duration (log t) at 1.40 V.

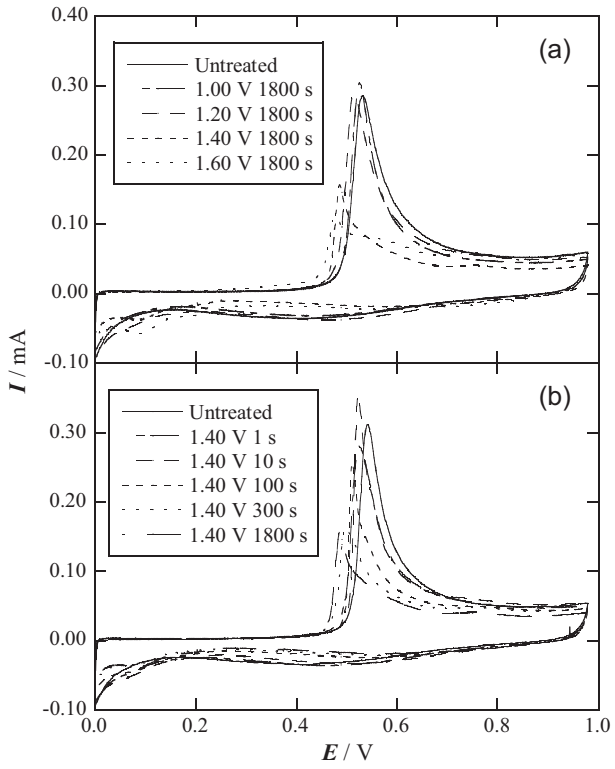

Fig. 3. Cyclic voltammograms for CO stripping on the HP 20% 1:1 Pt–Ru/C Vulcan XC-72 electrocatalyst anodically treated at: (a) the indicated anodic potentials during 1800 s and (b) 1.40 V for the marked times, in 0.5 M H_2SO_4 at 20 mV s^{-1} and 25.0 °C. CO was previously adsorbed during 15 min at 0.01 V. Catalyst ink with 30 μg Pt cm^{-2} and Nafion 30 wt.%.

potential and the duration of the anodic treatment produce changes in the voltammogram profile. The cyclic voltammogram shows a potential shift toward the hydrogen evolution regions. The hydrogen underpotential deposition (H_{upd}) region located in the range of 0.00–0.20 V is better observed and the adsorption peaks for the monoatomic hydrogen adsorption/desorption (at 0.07 V and at 0.17 V for (1 1 0) and (1 0 0) surfaces, respectively [41,42]) become clearly more visible. Since Ru shows a very low activity for H_{upd} [41], this behavior suggests a segregation of Ru atoms from the original Pt–Ru nanoparticles under the anodic treatment, originating a Pt enrichment on the catalytic surface. According to Fig. 1, this segregation is favored at higher applied potentials and longer treatment times.

In order to clarify the above-mentioned Ru segregation process, the evolution of the cathodic peak potential (E_p^c), corresponding to the reduction of the metallic oxides that are formed during the anodic scan, was analyzed. It is well known that the position of this peak is related in a linear way with the composition of Ru in the electrocatalyst nanoparticles [21]. As shown in Fig. 1, the reduction peak appears at 0.43 V in the untreated Pt–Ru/C electrocatalyst, being shifted to more positive values when the anodic potential or the duration of the anodic treatment rose. Fig. 2 presents such evolutions of E_p^c, thereby confirming the Ru-segregation process. It is observed in Fig. 2a that E_p^c achieves a plateau of 0.56 V when the anodic treatment was carried out at potential >1.40 V. An analogue trend is found when setting the potential at 1.40 V over 300 s, as can be seen in Fig. 2b. Since the expected E_p^c = 0.80 V for the Pt/C electrocatalyst is not achieved [42], the above tendencies suggest that the Ru-segregation is not complete under our working conditions. As long as the largest modification of E_p^c is only 0.13 V, in contrast with the shift of 0.37 V corresponding to 100% of the relative Ru segregation, one can conclude that the maximum relative amount of Ru segregation is about 35% and that most of the Ru atoms still remain on the surface of the nanoparticles.

3.2. CO stripping voltammetry after anodic treatment

Cyclic voltammograms for CO stripping experiments performed on the Pt–Ru/C electrocatalysts anodically treated at 1.00, 1.20, 1.40 and 1.60 V during 1800 s are shown in Fig. 3a. The corresponding voltammograms for different anodic treatment times (1, 10, 100, 300, and 1800 s) at 1.40 V are also displayed in Fig. 3b. Both figures denote that the anodic potential process modifies the CO oxidation activity of the electrocatalyst. To analyze the changes observed in the above trials, the electrochemically active surface area of the nanoparticles (ECSA) was determined. This was made by measuring the charge of CO stripping through integration between 0.40 and 0.80 V, subtracting the corresponding double layer charge, assuming a charge of 420 μC cm^{-2} for the oxidation of a monolayer of CO, and normalizing by the initial platinum loading [43].

The variation of ECSA (ΔECSA, in %) in front of the applied potential of the anodic treatment and the duration of the activation step is depicted in Fig. 4a and b, respectively. Both plots show a decrease of the active surface area after carrying out the potential treatment. Fig. 4a evidences minor ECSA losses between 1.00 and 1.20 V, but dramatic reductions of this parameter by about 50% when the anodic process involves potentials between 1.20 and 1.40 V, which become smaller again by rising the potential at 1.60 V. Fig. 4b shows a monotonic decay from 10% to 45% of the ECSA variation when the treatment time varies from 1 to 1800 s, thus indicating that the duration of the anodic step also strongly modifies the electrochemical behavior of the nanoparticles at 1.40 V. The ECSA reduction detected for the CO stripping trials of Fig. 4a and b could be related

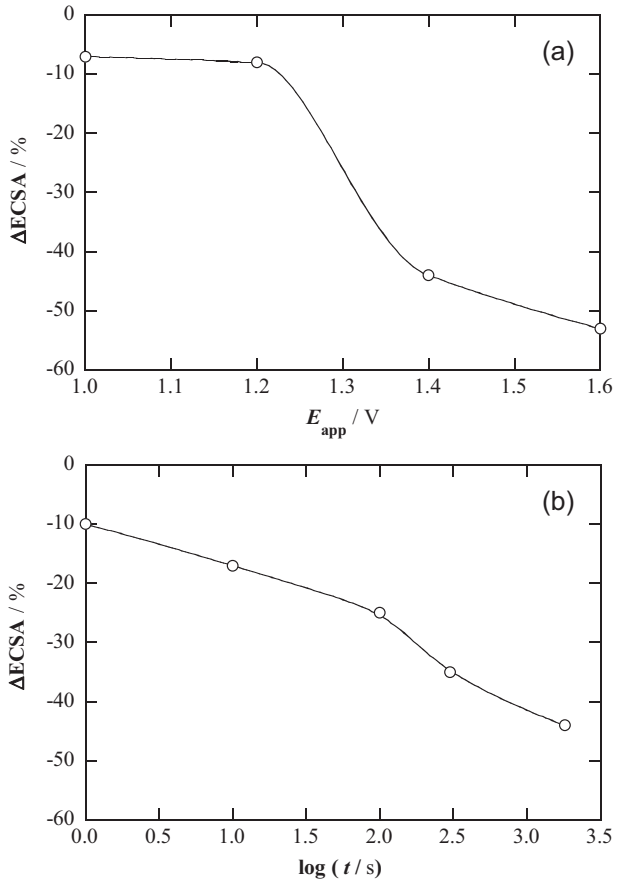

Fig. 4. Percentage of the change of the electrochemically active surface area vs. (a) the applied anodic potential during 1800 s and (b) the logarithm of the step potential duration at 1.40 V. Data from the cyclic voltammograms of Fig. 3.

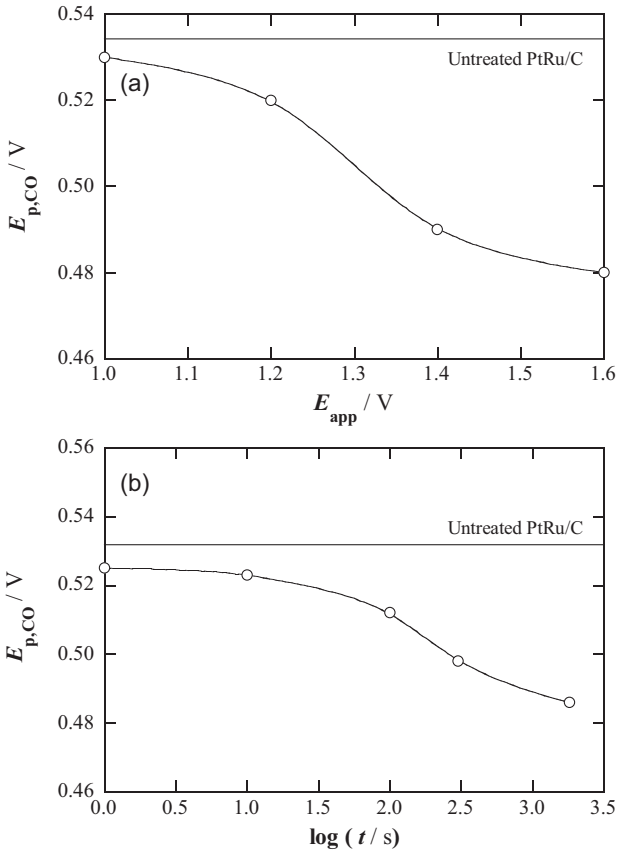

Fig. 5. Anodic peak potential for CO stripping in front of: (a) the applied anodic potential during 1800 s and (b) the logarithm of the step potential duration at 1.4 V. Data from the cyclic voltammograms of Fig. 3.

to the Ru-segregation, since it is well known that CO oxidation can also take place on Ru atoms [34]. However, the trends of Fig. 1 indicate that the Ru segregation from the nanoparticles surface is only produced in a fractional quantity and such loss may not explain the large reduction of the ECSA, even more considering that the final nanoparticles would exhibit a Pt-enriched surface. To clarify this point, the evolution of the anodic peak potential for CO stripping ($E_{p,CO}$) with the anodic treatment was analyzed.

The corresponding plots for $E_{p,CO}$ vs. the applied potential and the treatment time are presented in Fig. 5a and b, respectively. The $E_{p,CO}$ change toward less positive potentials observed in both cases is interpreted as an enhancement of the activity for the CO oxidation and, therefore, a better CO tolerance of the electrocatalyst. As can be seen in Fig. 5a, minor modifications of $E_{p,CO}$ are found when the anodically treatment is carried out at 1.00–1.20 V, causing a shift of 10 mV with respect the original CO stripping potential value. The main decrease of the anodic peak potential is observed again when 1.40 V is selected, giving a similar value at 1.60 V. Fig. 5b illustrates the existence of a significant decrease of $E_{p,CO}$ at times longer than 10 s at the selected potential of 1.40 V. After 1800 s, the CO stripping potential is located at 0.48 V, 50 mV less positive than that of the original Pt–Ru/C electrocatalyst. This apparent activation disagrees with the Ru-segregation process described above, because the Ru loss would lead to a decrease of the CO oxidation activity and $E_{p,CO}$ would be moved toward higher potentials. Therefore, the only explanation for achieving a better CO tolerance after the anodic treatment is the generation of some species more active for the promotion of CO oxidation that remain on the electrocatalyst surface. This species could be the hydrous ruthenium oxide RuO_xH_y, which can also be involved in the promotion of the CO oxidation as explained above. The water discharge on the RuO_xH_y sites takes place according to the following reaction [32]:

$$RuO_xH_y + H_2O \rightarrow RuO_{x+1}H_{y+1} + H^+ + e^- \quad (5)$$

where $RuO_{x+1}H_{y+1}$ represents the hydroxylated species formed on the oxide, in a similar way to that formed on Ru atoms in the original Pt–Ru/C electrocatalyst. It has been reported that RuO_xH_y has a better promotional effect than the alloyed Ru in Pt–Ru/C nanoparticles [32], so its presence in the electrocatalyst improves the CO tolerance. Our electrochemical results then suggest the segregation of Ru from the nanoparticles to create the RuO_xH_y moieties. This oxidation process starts at potentials >1.00 V and it is stimulated by prolonging the anodic treatment. Note that whereas Pt and Ru act as catalysts for CO oxidation, it has been reported that CO is not adsorbed on Ru oxides [35]. Therefore, a plausible contribution to the reduction of ECSA would be the production of RuO_xH_y on the nanoparticles surface, blocking the active sites for the CO oxidation. Another feature of special interest is that the cyclic voltammograms and CO stripping voltammograms shown in Figs. 1 and 3, respectively, were stationary after the anodic treatment, indicating that the generation of Ru oxides is an irreversible process and these species are not further reduced to regenerate the original structure. The morphological changes induced by the anodic treatment will be discussed below.

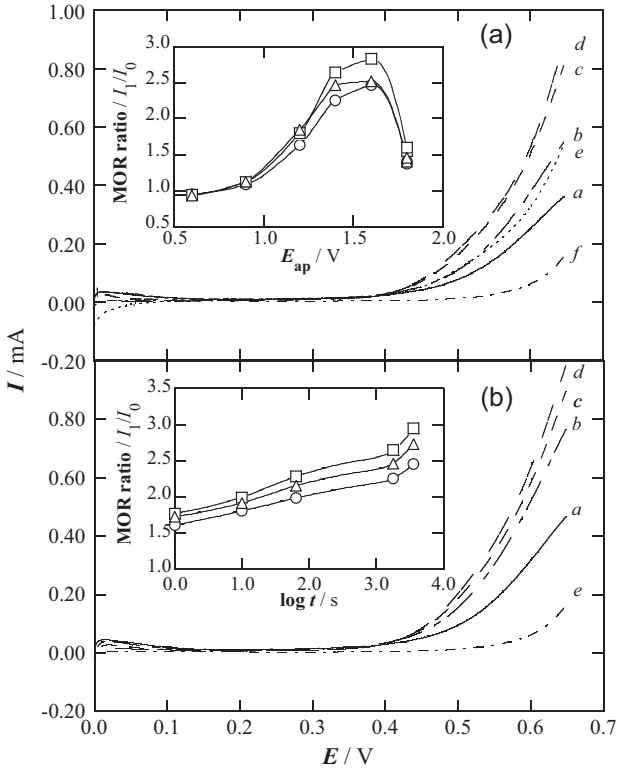

Fig. 6. Cyclic voltammograms (only the anodic swept is shown) for the methanol oxidation reaction (MOR) on the HP 20% 1:1 Pt–Ru/C Vulcan XC-72 electrocatalyst. In plot (a), the electrocatalyst was anodically treated during 1800 s at (*b*) 1.20 V, (*c*) 1.40 V, (*d*) 1.60 V and (*e*) 1.80 V. The polarization curves corresponding to the MOR on (*a*) the untreated HP 20% 1:1 Pt–Ru/C Vulcan XC-72 electrocatalyst and (*f*) the HP 20% Pt/C Vulcan XC-72 specimen are also displayed. The inset panel shows the ratio of the MOR current before (I_0) and after (I_1) the anodic treatment vs. the applied potential for 1800 s at (○) 0.45 V, (□) 0.50 V and (Δ) 0.55 V. In plot (b), anodic treatment of the electrocatalyst at 1.40 V for (*b*) 1 s, (*c*) 65 s and (*d*) 3600 s. Results for the MOR on (*a*) the untreated HP 20% 1:1 Pt–Ru/C Vulcan XC-72 electrocatalyst and (*f*) the HP 20% Pt/C Vulcan XC-72 specimen are also presented. The inset panel shows the I_1/I_0 ratio in front of log *t* at (○) 0.45 V, (□) 0.50 V and (Δ) 0.55 V. Data collected at 20 mV s^{-1} and 25.0 °C. Catalyst ink with 30 μg Pt cm^{-2} and Nafion 30 wt.%.

3.3. Influence of anodic treatment in the methanol oxidation reaction

The anodic scans of the cyclic voltammograms recorded for the MOR on the electrocatalyst without treatment and anodically treated at 1.00, 1.20, 1.40, 1.60, and 1.80 V for 1800 s are presented in Fig. 6a. Fig. 6b displays the analogous curves registered for the Pt–Ru/C specimen as received and after anodic treatment at 1.40 V during 1, 65, and 3600 s. For comparison purposes, both plots also show the voltammogram corresponding to MOR on the Pt/C electrocatalyst. The onset potential for the alcohol oxidation is reduced from 0.50 to 0.35 V when the pure Pt and the alloyed electrocatalysts are compared. This shifting toward a less positive potential is usually explained by the bifunctional mechanism model, which postulates that the intermediate carbonaceous species formed through the methanol oxidation, with general structure CH_xO, are more easily oxidized with the help of the Ru hydroxylated species.

The influence of the selected potential for the anodic treatment is better analyzed from the data of the inset panel of Fig. 6a, which presents the ratio for the MOR current obtained after and before the anodic treatment (I_1 and I_0, respectively) in front of the applied potential for 1800 s. When 0.60 V was intended as the activation potential, no increase in the MOR current was detected ($I_1/I_0 \approx 1.00$), obtaining a similar performance to the corresponding control experiment (without anodic treatment). However, a clear promotional effect starts to happen for applied potentials >0.80 V, achieving a maximum at 1.40–1.60 V ($I_1/I_0 = 2.5$–2.7). Note that this enhancement is close to that obtained in our previous work [39] by potential cycling of the Pt–Ru/C electrocatalyst with 1.00 V as anodic limit. However, when a superior potential of 1.80 V is applied, the MOR current is significantly decreased. This trend can be explained by assuming that the RuO_xH_y generation causes the activation, that is, as in the case of the CO oxidation reaction, this hydrous oxide can also promote the MOR. In fact, CO is involved in the alcohol oxidation as key intermediate in the rate-determining step of the reaction pathway [39], so it is coherent to assume the MOR activation in a similar way to that of the CO oxidation. In this series of experiments, the increase in the MOR current suggests that the Ru oxidation to form the RuO_xH_y is dominant at potentials >1.00 V, similarly to the trend found for the CO oxidation (Fig. 5b).

The existence of the highest performance region at 1.40–1.60 V and the subsequent decrease of the activity at superior potentials can be explained if the generation of the Ru oxide blocks Pt sites for the MOR, as proposed in the case of the CO stripping analysis of Fig. 4. Therefore, a balance between the promotional effect of RuO_xH_y and the ECSA decrease takes place. There is also the possibility of the dissolution of the beneficial Ru oxide at high potential, which would also produce the diminution of the alcohol oxidation current. Amorphous Ru oxide has been reported to be more susceptible to the dissolution than alloyed Ru [20]. Besides, at high working potentials the oxygen evolution must be taken into account, since the gas evolution could cause the release of catalyst loading with the consequent decrease of the MOR performance. Therefore, potentials >1.60 V should be avoided. In addition, oxidation of the carbon support due to the anodic treatment must be also considered. According to PEFCs lifetime analysis [44], the fuel cell performance decreases with the oxidation of the carbon support at high potentials ($E > 1.00$ V) and the temperature favors this corrosion process. The generation of oxygen-containing functional groups (—COOH, —C═O, —OH, etc.) decreases the conductivity of the electrocatalysts and also originates a weakening of the interaction with the nanoparticles. However, these effects are more relevant when the anodic treatment is carried out by potential cycling [44]. In the case of steady-state polarization, as we have performed in this work, the effects are smaller. Note that the oxidation of carbon to CO_2 or CO is not kinetically favored, but it can also be significant at high potentials, contributing to the low MOR current obtained at $E > 1.60$ V.

The inset panel of Fig. 6b shows the gradual increase in MOR ratio with prolonging anodic treatment time, as expected by the progressive formation of more RuO_xH_y. Note that even with an anodic treatment time as short as 1 s is possible to achieve an improvement of the MOR current of 60–70%. However, no significant catalytic changes for methanol oxidation were found for times >1800 s, indicating that the main parameter affecting the activation of the Pt–Ru/C electrocatalyst is the potential selected for the anodic treatment.

Note that fuel cell voltage is normally in the range 0.5–0.8 V and the anode potential depends on the operating conditions. Therefore, to assure the formation of the beneficial RuO_xH_y in a given fuel cell with a Pt–Ru anode, an anodic pretreatment of the membrane electrode assembly (MEA) with a controlled anode potential could be necessary, for example before building up the fuel cell package.

Previous works using RDE [39] and steady-state polarization techniques [45] reported that MOR was not influenced by mass transfer in the present conditions, so the classical Tafel expression of *E* vs. log *I* [46] was used to analyze the *I*–*E* data obtained directly from cyclic voltammogram, as reported elsewhere [47]. Fig. 7a and b depicts the corresponding Tafel plots obtained from Fig. 6a and b. These plots were made in the potential range under charge-transfer

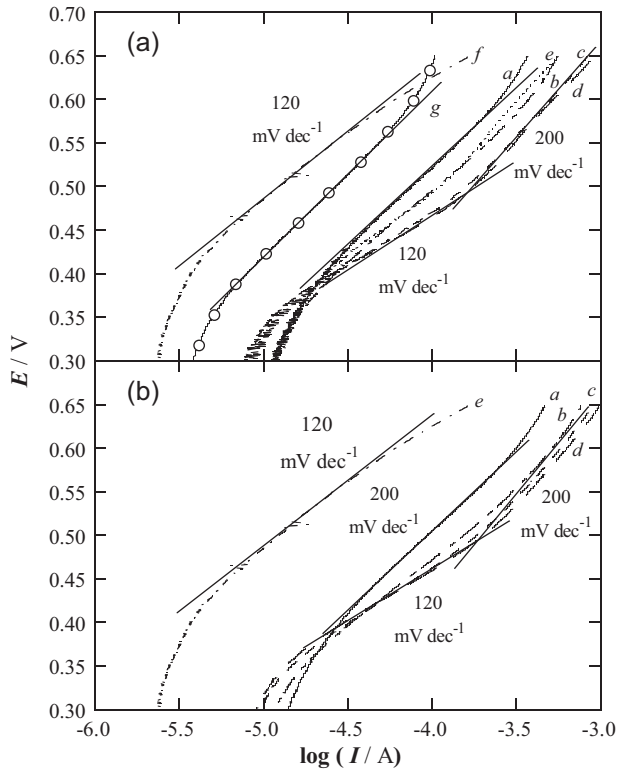

Fig. 7. Apparent Tafel slopes built up from the MOR polarization curves of: (a) Fig. 6a and (b) Fig. 6b. The result obtained for the MOR on the HP 20% 1:1 Pt–Ru/C Vulcan XC-72 electrocatalyst employing potentiodynamic polarization at 1.0 mV s^{-1} is also presented (curve *g* in a) for comparison purposes.

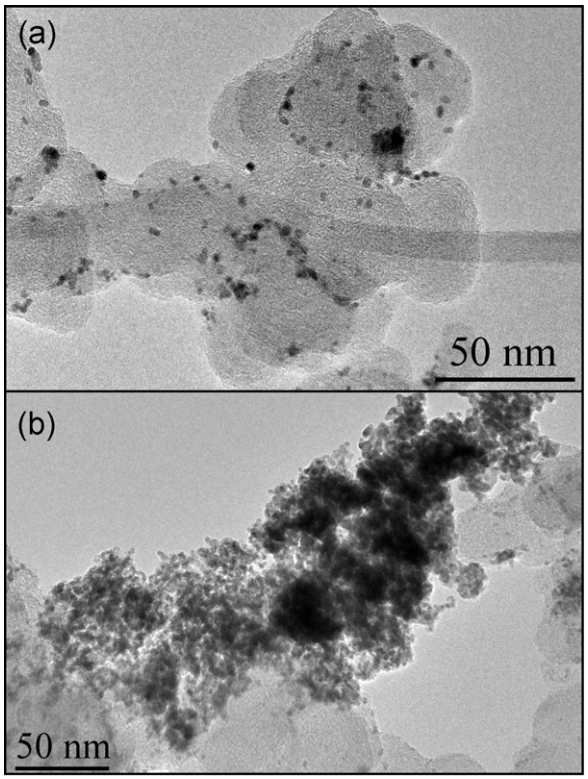

Fig. 8. TEM images showing (a) the metallic nanoparticles on the carbon surface and (b) the formation of agglomerates on the HP 20% 1:1 Pt–Ru/C Vulcan XC-72 electrocatalyst anodically treated at 1.40 V during 1800 s.

control and Tafel slopes of 120 mV dec^{-1} ($\alpha = 0.5$) and 200 mV dec^{-1} ($\alpha = 0.3$) for the MOR on the original Pt/C and Pt–Ru/C electrocatalysts, respectively, were obtained. Potentiostatic polarization (curve *g* in Fig. 7a) was also used in order to corroborate that MOR is not altered by mass-transfer effects and the same Tafel slope of 200 mV dec^{-1} was obtained for the untreated Pt–Ru/C electrocatalyst. This value is in agreement with that reported by Gasteiger et al. [15], who found a Tafel slope of 180 mV dec^{-1} working at 60 °C for the MOR on bulk Pt–Ru alloys, and by Martínez et al. [48], who reported a Tafel slope of also 200 mV dec^{-1} for the alcohol oxidation on the Pt/MoW electrocatalyst.

According to Fig. 7, for the anodically treated specimen, two apparent Tafel slopes were found when the anodic treatment was made at 1.40–1.60 V, also with values of 120 and 200 mV dec^{-1}, the latter at higher overpotentials. Note that, as shown in Fig. 2, the different anodic treatments lead to different Ru segregation, as it is explained in Section 3.1, thus indicating the formation of different Pt–Ru oxides. In addition, the activation of the methanol oxidation appears to be related to the modification of the Tafel plots from one to two apparent Tafel lines. Therefore, the presence of two apparent Tafel slopes after the anodic treatment can be tentatively explained considering that the alcohol is oxidized on two kinds of active sites. Thus, the apparent Tafel slope of 200 mV dec^{-1} (the same value as found for the untreated specimen) can be attributed to the MOR on the Pt–Ru moieties that remain on the electrocatalyst, whereas the apparent Tafel slope of 120 mV dec^{-1} could be caused by the methanol oxidation on Pt sites surrounded by RuO_xH_y. However, one could also think that this latter apparent Tafel slope is due to the MOR on Pt free sites, so the existence of the hydrous oxide is not required. Nevertheless, some reasons justify the presence of Pt–RuO_xH_y active sites in the electrocatalyst. Firstly, Fig. 6 illustrates that the onset potential for the MOR does not change toward higher positive values with the anodic treatment, which would be the logical result of a Ru loss from the electrocatalyst. On the other hand, the apparent Tafel slope of 120 mV dec^{-1} is better defined when the potential of the anodic treatment and the duration of the step increase, as observed in Fig. 6a and b respectively, and both situations lead to a larger formation of Ru oxide, as commented above from the CO stripping results. Finally, note that this apparent Tafel slope appears at a lower overpotential region than that of the MOR on the original Pt–Ru/C sites. This suggests the formation of a new kind of catalytic surface involving a species more active for the MOR than the Ru atoms, as it is the case of the RuO_xH_y. It is also of special interest that the double-Tafel region practically disappears when the anodic potential of 1.80 V is applied (curve *e* in Fig. 7a), showing only the characteristic value of 200 mV dec^{-1}. This behavior matches with the observed decrease in the MOR current at this selected potential in Fig. 6a. Thus, the suppression of the apparent Tafel slope of 120 mV dec^{-1} appears to be related to the partial loss of the RuO_xH_y moieties by Ru dissolution at high applied potentials.

However, although the experimental data support the model of two different active sites for the MOR, alternative explanations to the proposed one for the existence of two apparent Tafel regions are also plausible, such as the change of the coverage conditions of the species involved in the alcohol oxidation (methanol residues, hydroxylated species, etc.), the modification of the reaction mechanism or the existence of a potential dependence for the Tafel slope.

3.4. Structural analyses

The morphological study of the anodically treated Pt–Ru/C electrocatalyst was carried out using TEM. The analysis was focused in the specimen treated at 1.40 V during 1800 s, which presents the best performance for the methanol oxidation. Its

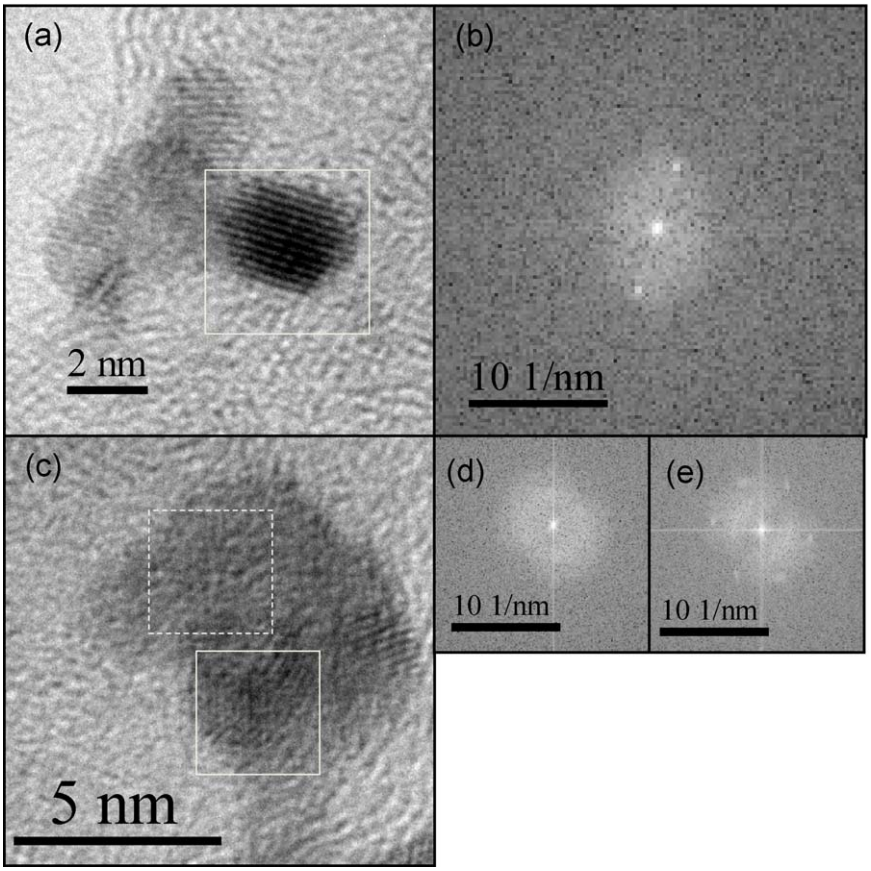

Fig. 9. (a) HRTEM image for HP 20% 1:1 Pt–Ru/C Vulcan XC-72 electrocatalyst anodically treated at 1.40 V during 1800 s and (b) FFT obtained for the analysis of the marked nanoparticle. (c) HRTEM image highlighting two areas where FFT is applied revealing: (d) no signals (amorphous structure, dotted line region) and (e) crystalline Pt planes (solid line region).

characteristic TEM images are shown in Fig. 8a, while an example of the agglomeration of metallic nanoparticles, also found in the sample, is depicted in Fig. 8b. The morphology exhibited in Fig. 8a is similar to that described for the untreated Pt–Ru/C electrocatalyst [49], showing a good dispersion of the nanoparticles. However, the presence of metallic agglomerates after the potential step was observed (Fig. 8b). It can then be suggested that the anodic treatment produces a loss of contact between the nanoparticles and the carbon surface, so most of them are released and become aggregated. Note that this agglomeration would also contribute to the reduction of the ECSA that was detected in the CO stripping experiments. As long as ΔECSA is due to segregation and agglomeration, the ΔECSA value at 1.4 V after 300 s, shown in Fig. 4b, has not to be necessarily coincident with that value after 1800 s, in spite of similar Pt:Ru ratio for both potential step durations (Fig. 2b). Moreover, the long-term operation experiments could be comparable to the fuel cell performance after a continued working period, which is known that produces the agglomeration of the electrocatalyst components [20]. The morphology exhibited in Fig. 8 is also in agreement with the results reported by PEFCs analysis after performance at oxidizing conditions [44], where the weakening of the nanoparticles-carbon support bond was also detected. Other possible contributions to this morphology such as the ultrasonic treatment made for the sample preparation can be discarded, since no agglomerates were detected in control experiments with the untreated electrocatalyst following the same procedure. In conclusion, the main factor yielding to the observed structure must be the anodic treatment.

EDX analyses were made to determine the elemental composition of the above anodically treated specimen at 1.40 V. According to the relation of the peak areas of the elements in the EDX analyses before and after the anodic treatment, no Pt losses were detected, whereas the Pt:Ru atomic ratio slightly changed to 54:46. This ratio is quite close to the original composition (50:50, also proved by EDX), indicating that the anodic treatment at 1.40 V produces only a minimum Ru loss and most of the metal is still present, probably as hydrous Ru oxide, as previously proposed [33]. On the other hand, these results indicate that the overall metal loading after the anodic treatment was close to the original metal/carbon relationship provided by the company.

The FFT algorithm was employed in the elucidation of the crystalline phases formed in the electrocatalyst. Fig. 9a and b shows a high-resolution TEM image of a metallic nanoparticle and the corresponding FFT applied to the selected region, respectively. The interplanar distance of 0.22 nm is attributed to the Pt face cubic centered (FCC) unit cell, which also contains part of the Ru atoms. This structure was the only crystallographic phase found using this methodology, indicating that the Pt–Ru alloy is still the main ordered phase in the electrocatalyst. This result is in agreement with the FFT results obtained for the untreated Pt–Ru/C specimen [49], in which the Pt crystalline structure of the nanoparticles was dominant (Pt_3O_4 and PtO_2 were also detected in a minor level). On the other hand, Fig. 9c shows that some of the crystalline nanoparticles seem to be surrounded by amorphous material. The FFT results corresponding to the marked regions are shown in Fig. 9d and e. Again, typical interplanar distances for Pt cell are obtained. The nature of the amorphous structure cannot be fully understood only by TEM, but it most probably contains amorphous RuO_xH_y. In fact, the existence of amorphous material containing RuO_xH_y was previously found by the authors in the same untreated Pt–Ru/C

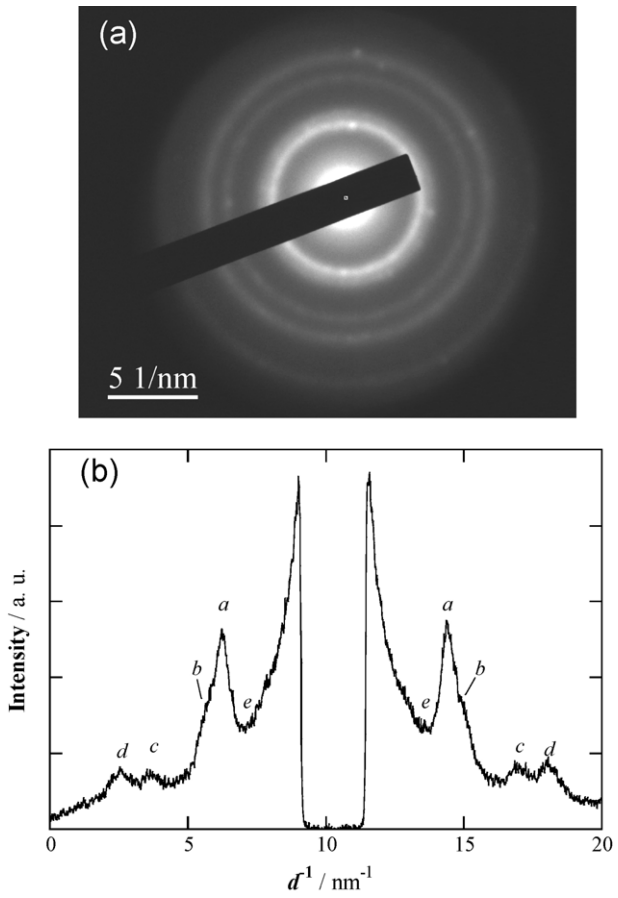

Fig. 10. (a) Selected-area electron diffraction (SAED) of a representative region of the HP 20% 1:1 Pt–Ru/C Vulcan XC-72 electrocatalyst anodically treated at 1.40 V during 1800 s. (b) Diffraction intensity profile with signals attributed to (*a* and *c*) Pt/Ru oxides and (*b* and *d*) Pt.

electrocatalyst using TEM, XRD, and XPS [38]. According to the electrochemical data, this amorphous phase should correspond to the metallic oxides that are generated through the anodic treatment, including the beneficial RuO_xH_y. As it is observed, this structure is in close contact with the crystalline nanoparticles and hence, it is the configuration that would cause the improvement of the CO and the methanol oxidations and also the reduction of the ECSA. A similar framework has been previously suggested from TEM observations [22,34] and XRD data interpretation [20,29].

SAED was finally used to complete the structural study of the anodically treated electrocatalyst. Fig. 10a shows the characteristic diffraction signals of the present species. To clarify the different contributions to this diffractogram, the diffraction intensity profile was built and presented in Fig. 10b. The interplanar distances *b* (0.22 nm) and *d* (0.12 nm) can be attributed to the presence of metallic Pt, as confirmed by FFT analysis, corresponding to the (1 1 1) and (1 1 3) planes, respectively. In the case of the signals *a* and *c*, the interpretation is not trivial. Thus, in the case of the interplanar distance *a* (0.25 nm), this value is well-matched with the planes (1 0 1) and (0 1 1) of PtO_2, (2 1 0) of Pt_3O_4 and (1 0 1) of RuO_2. For the interplanar distance *c* (0.15 nm), the planes (3 2 0) and (3 2 1) of Pt_3O_4 and (2 2 0) of RuO_2 could be associated. These findings confirm that metallic oxides exist on the anodically treated electrocatalyst. Note that the SAED pattern for the untreated Pt–Ru/C electrocatalyst also revealed diffraction signals attributed to PtO_2 and Pt_3O_4 species, as we reported in our previous work [49], so a combination of original and produced metallic oxides explain the observed diffraction pattern. On the other hand, the most intense diffraction signal for the RuO_2 phase should correspond to the planes (1 1 0) with an interplanar distance of 0.32 nm, which was observed as a very weak signal in the position *e* of Fig. 10b, suggesting that this oxide is present mainly with an amorphous structure. Note that its hydrated form is the beneficial RuO_xH_y. The proposed morphology from SAED analysis of Fig. 10 matches with the framework exhibited in the TEM image of Fig. 9c.

Although all these techniques together with the electrochemical experiments were found to be suitable tools for accurately interpreting the structural changes produced, we tried to confirm by XPS the formation of additional RuO_xH_y during the anodic treatment (already present in the untreated specimen [38]). However, the amount of catalyst collected from the electrode was too small and no peaks were distinguishable from the background signal, neither in the Ru region, nor in the Pt region. For this reason, further experiments involving more amounts of catalyst and different techniques are planned to determine the quantity of additional RuO_xH_y formed during the anodic treatment.

4. Conclusions

A Pt–Ru/C electrocatalyst was submitted to anodic treatment using steady-state polarizations at potentials over 1.0 V vs. RHE with different step durations. Cyclic voltammograms in 0.5 M H_2SO_4 showed an evolution of the H_{upd} region toward a Pt profile, thus suggesting some kind of Ru segregation during the treatment. The analysis of the cathodic peak potential corresponding to the reduction of metallic oxides indicated that this segregation was incomplete. Stripping experiments revealed that the oxidation potential of CO was moved toward lower values after the anodic potential step, thus indicating an activation of the electrocatalyst. The simultaneous reduction of the ECSA was assigned to the formation of Pt/Ru oxides on the nanoparticles surface, inactive for CO oxidation and to some carbon oxidation with agglomeration of nanoparticles. By comparing the electrocatalyst performance for methanol oxidation before and after the anodic treatment, the optimum potential range was found to be in the range 1.40–1.60 V, with an increase in the MOR current of about 2.5–2.7 times the initial one. The activation of CO oxidation and MOR was explained by the generation of the RuO_xH_y active species.

The kinetic analysis of the alcohol oxidation in the anodically activated electrocatalyst showed two apparent Tafel slopes, with values of 120 and 200 mV dec^{-1}, the latter for the highest overpotential region. This was explained by the existence of two kinds of active sites for the MOR, related both to the remaining Pt–Ru sites and the generated Pt–RuO_xH_y moieties.

The anodic treatment at 1.80 V produced a dramatic decrease in the MOR performance, which was attributed to the dissolution of the RuO_xH_y moieties together with a loss in the catalyst loading because of the intense oxygen evolution at this potential and the carbon oxidation.

The TEM study after the anodic treatment revealed that the potential step causes some nanoparticle agglomeration. The EDX analyses showed a minimum Ru loss in the case of the best anodically treated electrocatalyst for methanol oxidation, the Pt:Ru ratio remaining close to the original relationship. FFT analyses revealed Pt FCC as the main crystallographic phase in the electrocatalyst and some amorphous structures, assigned to Pt/Ru oxides including RuO_xH_y, formed during anodic treatment, near the crystalline nanoparticles. The SAED technique allowed confirming the existence of Pt as the main crystallographic structure, although diffraction signals for metallic oxides such as PtO_2, Pt_3O_4 or RuO_2 were also detected. All these results suggest that an anodic pretreatment of the membrane electrode assembly (MEA) with a Pt–Ru/C

electrocatalyst before building the fuel cell package will improve its performance.

Acknowledgments

The authors thank the financial support given by the Spanish MEC (Ministerio de Educación y Ciencia) through the project NAN2004-09333-C05-03. The FPU fellowship from Spanish MEC received by A. Velázquez to do this work is also acknowledged. The authors also thank the CCiT-UB (Scientific and Technological Centers of the Universitat de Barcelona) for the structural analysis facilities. This work is dedicated to the memory of Amado Velázquez Méndez.

References

[1] F. Alcaide, P.L. Cabot, E. Brillas, J. Power Sources 153 (2006) 47–60.
[2] C. Alegre, L. Calvillo, R. Moliner, J.A. González-Expósito, O. Guillén-Villafuerte, M.V. Martínez Huerta, E. Pastor, M.J. Lázaro, J. Power Sources 196 (2011) 4226–4235.
[3] A. Bauer, K. Lee, C. Song, Y. Xie, J. Zhang, R. Hui, J. Power Sources 195 (2010) 3105–3110.
[4] H.A. Gasteiger, J.E. Panels, S.G. Yan, J. Power Sources 127 (2004) 162–171.
[5] R. Rego, M. Cristina, F. Oliveira, I. Esparbé, P.L. Cabot, J. Power Sources 189 (2009) 1120–1126.
[6] J.R.C. Salgado, F. Alcaide, G. Álvarez, L. Calvillo, M.J. Lázaro, E. Pastor, J. Power Sources 195 (2010) 4022–4029.
[7] N. Tsiouvaras, M.V. Martínez-Huerta, R. Moliner, M.J. Lázaro, J.L. Rodríguezb, E. Pastor, M.A. Peña, J.L.G. Fierro, J. Power Sources 186 (2009) 299–304.
[8] L. Zhang, J. Kim, H.M. Chen, F. Nan, K. Dudeck, R.S. Liu, G.A. Botton, J. Zhang, J. Power Sources 196 (2011) 9117–9123.
[9] T. Iwasita, in: W. Vielstich, A. Lamm, H.A. Gasteiger (Eds.), Handbook of Fuel Cells—Fundamentals, Technology and Applications, John Wiley & Sons, New York, 2003, pp. 603–622.
[10] E.I. Santiago, V.A. Paganin, M. Do Carmo, E.R. Gonzalez, E.A. Ticianelli, J. Electroanal. Chem. 575 (2005) 53–60.
[11] T. Vidakovic, M. Christov, K. Sundmacher, J. Electroanal. Chem. 580 (2005) 105–121.
[12] K. Ruth, M. Vogt, R. Zuber, in: W. Vielstich, A. Lamm, H.A. Gasteiger (Eds.), Handbook of Fuel Cells—Fundamentals Technology and Applications, John Wiley & Sons, New York, 2003, pp. 489–496.
[13] S. Alayoglu, A.U. Nilekar, M. Mavrikakis, B. Eichhorn, Nat. Mater. 7 (2008) 333–338.
[14] A.S. Arico, P.L. Antonucci, E. Modica, V. Baglio, H. Kim, V. Antonucci, Electrochim. Acta 47 (2002) 3723–3732.
[15] H.A. Gasteiger, N. Markovic, P.N. Ross Jr., E.J. Cairns, J. Electrochem. Soc. 141 (1994) 1795–1803.
[16] T. Iwasita, H. Hoster, A. John-Anacker, W.F. Lin, W. Vielstich, Langmuir 16 (1999) 522–529.
[17] H.T. Kim, H.I. Joh, S.H. Moon, J. Power Sources 195 (2010) 1352–1358.
[18] W.H. Lizcano-Valbuena, V.A. Paganin, E.R. Gonzalez, Electrochim. Acta 47 (2002) 3715–3722.
[19] Z.G. Shao, F. Zhu, W.F. Lin, P.A. Christensen, H. Zhang, J. Power Sources 161 (2006) 813–819.
[20] W. Chen, G. Sun, Z. Liang, Q. Mao, H. Li, G. Wang, Q. Xin, H. Chang, C. Pak, D. Seung, J. Power Sources 160 (2006) 933–939.
[21] T. Frelink, W. Visscher, J.A.R. Van Veen, Langmuir 12 (1996) 3702–3708.
[22] L. Gan, H. Du, B. Li, F. Kang, J. Power Sources 191 (2009) 233–239.
[23] S.L. Gojkovic, T.R. Vidakovic, D.R. Durovic, Electrochim. Acta 48 (2003) 3607–3614.
[24] J.L. Gómez de la Fuente, M.V. Martínez-Huerta, S. Rojas, P. Hernández-Fernández, P. Terreros, J.L.G. Fierro, M.A. Peña, Appl. Catal. B: Environ. 88 (2009) 505–514.
[25] S.Y. Huang, C.T. Yeh, J. Power Sources 195 (2010) 2638–2643.
[26] M.K. Jeon, P.J. McGinn, J. Power Sources 188 (2009) 427–432.
[27] Y.Y. Liang, H.L. Li, X.G. Zhang, J. Power Sources 173 (2007) 599–605.
[28] Q. Lu, B. Yang, L. Zhuang, J. Lu, J. Phys. Chem. B 109 (2005) 1715–1722.
[29] J.H. Ma, Y.Y. Feng, J. Yu, D. Zhao, A.J. Wang, B.Q. Xu, J. Catal. 275 (2010) 34–44.
[30] F. Peng, C. Zhou, H. Wang, H. Yu, J. Liang, J. Yang, Catal. Commun. 10 (2009) 533–537.
[31] B.R. Rauhe Jr., F.R. McLarnon, E.J. Cairns, J. Electrochem. Soc. 142 (1995) 1073–1084.
[32] D.R. Rolison, P.L. Hagans, K.E. Swider, J.W. Long, Langmuir 15 (1999) 774–779.
[33] A. Rose, E.M. Crabb, Y. Qian, M.K. Ravikumar, P.P. Wells, R.J.K. Wiltshire, J. Yao, R. Bilsborrow, F. Mosselmans, A.E. Russell, Electrochim. Acta 52 (2007) 5556–5564.
[34] F. Scheiba, M. Scholz, L. Cao, R. Schafranek, C. Roth, C. Cremers, X. Qiu, U. Stimming, H. Fuess, Fuel Cells 6 (2006) 439–446.
[35] W. Sugimoto, T. Saida, Y. Takasu, Electrochem. Commun. 8 (2006) 411–415.
[36] K.E. Swider, C.I. Merzbacher, P.L. Hagans, D.R. Rolison, Chem. Mater. 9 (1997) 1248–1255.
[37] S.C. Thomas, X. Ren, S. Gottesfeld, J. Electrochem. Soc. 146 (1999) 4354–4359.
[38] A. Velázquez-Palenzuela, F. Centellas, J.A. Garrido, C. Arias, R.M. Rodríguez, E. Brillas, P.L. Cabot, J. Phys. Chem. C 114 (2010) 4399–4407.
[39] A. Velázquez-Palenzuela, F. Centellas, J.A. Garrido, C. Arias, R.M. Rodríguez, E. Brillas, P.L. Cabot, J. Power Sources 196 (2011) 3503–3512.
[40] T.J. Schmidt, H.A. Gasteiger, in: W. Vielstich, A. Lamm, H.A. Gasteiger (Eds.), Handbook of Fuel Cells—Fundamentals, Technology and Applications, John Wiley & Sons, New York, 2003, pp. 316–333.
[41] H.A. Gasteiger, N.M. Markovic, P.N. Ross Jr., J. Phys. Chem. 99 (1995) 8290–8301.
[42] I. Esparbé, E. Brillas, F. Centellas, J.A. Garrido, R.M. Rodríguez, C. Arias, P.L. Cabot, J. Power Sources 190 (2009) 201–209.
[43] L. Dos Santos, F. Colmati, E.R. Gonzalez, J. Power Sources 159 (2006) 869–877.
[44] B. Avasarala, R. Moore, P. Haldar, Electrochim. Acta 55 (2010) 4765–4771.
[45] J.M. Sieben, M.M.E. Duarte, C.E. Mayer, Int. J. Hydrogen Energy 35 (2010) 2018–2024.
[46] G. Tremiliosi-Filho, H. Kim, W. Chrzanowski, A. Wieckowski, B. Grzybowska, P. Kulesza, J. Electroanal. Chem. 467 (1999) 143–156.
[47] P. Hernández-Fernández, R. Nuño, E. Fatás, J.L.G. Fierro, P. Ocón, Int. J. Hydrogen Energy 36 (2011) 8267–8278.
[48] S. Martínez, M.E. Martins, C.F. Zinola, Int. J. Hydrogen Energy 35 (2010) 5343–5355.
[49] A. Velázquez, E. Brillas, F. Centellas, J.A. Garrido, R.M. Rodríguez, C. Arias, P.L. Cabot, J. Power Sources 195 (2010) 710–719.